



HAL
open science

Advanced and Integrated Petrophysical Characterization for CO₂ Storage: Application to the Ketzin Site.

Marc Fleury, Serge Gautier, Nicolas Gland, Pierre Boulin, B. Norden

► **To cite this version:**

Marc Fleury, Serge Gautier, Nicolas Gland, Pierre Boulin, B. Norden. Advanced and Integrated Petrophysical Characterization for CO₂ Storage: Application to the Ketzin Site.. Oil & Gas Science and Technology - Revue d'IFP Energies nouvelles, 2013, 68 (3), pp.557-576. 10.2516/ogst/2012084 . hal-00864230

HAL Id: hal-00864230

<https://ifp.hal.science/hal-00864230>

Submitted on 20 Sep 2013

HAL is a multi-disciplinary open access archive for the deposit and dissemination of scientific research documents, whether they are published or not. The documents may come from teaching and research institutions in France or abroad, or from public or private research centers.

L'archive ouverte pluridisciplinaire **HAL**, est destinée au dépôt et à la diffusion de documents scientifiques de niveau recherche, publiés ou non, émanant des établissements d'enseignement et de recherche français ou étrangers, des laboratoires publics ou privés.

Advanced and Integrated Petrophysical Characterization for CO₂ Storage: Application to the Ketzin Site

M. Fleury^{1*}, S. Gautier¹, N. Gland¹, P.F. Boulon¹, B. Norden²
and C. Schmidt-Hattenberger²

¹ IFP Energies nouvelles, 1-4 avenue de Bois-Préau, 92852 Rueil-Malmaison - France

² GFZ German Research Centre for Geosciences, Helmholtz Centre Potsdam - Germany
e-mail: marc.fleury@ifpen.fr

* Corresponding author

Résumé — Caractérisation pétrophysique intégrée pour le stockage de CO₂ : application au site de Ketzin — La simulation et le suivi d'un stockage de CO₂ requiert des données pétrophysiques spécifiques. Nous présentons un ensemble d'expériences applicables à tout stockage et à toute couverture, fournissant des données pour des simulations numériques réalistes du potentiel de stockage et de l'injection. Ces expériences sont intégrées avec les données diagraphiques pour l'estimation de la porosité, la saturation irréductible, la pression capillaire et la perméabilité relative de l'eau en drainage, la saturation en gaz résiduelle, les relations résistivité-saturation et les propriétés de transport de la couverture (perméabilité et diffusivité). Le cas considéré est l'aquifère salin du Trias dans le contexte du projet CO₂SINK, le premier site expérimental de stockage en Allemagne situé près de Ketzin.

Nous avons utilisé des méthodes de mesure nécessitant des durées raisonnables tout en restant représentatives des processus *in situ*. Pour le transport diphasique, nous avons utilisé la centrifugation. Pour la résistivité, nous avons utilisé une méthode rapide « *Fast Resistivity Index Measurement* » (FRIM) en drainage et imbibition, en condition ambiante et en condition de stockage. Pour la caractérisation de la couverture, nous avons utilisé une technique rapide RMN (Résonance Magnétique Nucléaire) utilisant le deutérium comme traceur pour la mesure de diffusion et une méthode stationnaire innovante pour la mesure de perméabilité. La pression d'entrée a également été évaluée. Les diagraphies RMN et de résistivité ont également été utilisées pour estimer de manière continue la saturation irréductible et juger de la représentativité des échantillons analysés au laboratoire.

Pour le site de Ketzin, la zone de stockage est un grès argileux d'origine fluvatile localement très cimenté d'une porosité d'environ 30 % et d'une perméabilité variant de 100 à 300 mD. Deux zones se distinguent par des saturations irréductibles variant de 15 à 35 %. La courbe de perméabilité relative à l'eau présente une forte pente et suggère qu'une saturation inférieure à 50 % n'est pas atteignable en pratique. L'exposant de saturation de l'indice de résistivité est de 1,7, plus faible que la valeur standard de 2. La couverture a une perméabilité de 27 nD, une porosité de 15 % et une diffusivité de $0,8 \times 10^{-9}$ m²/s.

Abstract — Advanced and Integrated Petrophysical Characterization for CO₂ Storage: Application to the Ketzin Site — Reservoir simulations and monitoring of CO₂ storage require specific petrophysical data. We show a workflow that can be applied to saline aquifers and caprocks in order to provide the minimum data set for realistic estimations of storage potential and perform pertinent simulations of CO₂ injection. The presented series of experiments are fully integrated with quantitative log data analysis to estimate porosity, irreducible saturation, drainage capillary pressure and water relative permeability, residual gas saturation, resistivity-saturation relationships and caprock transport properties (permeability and diffusivity). The case considered is a saline aquifer of the Triassic Stuttgart formation studied in the framework of the CO₂SINK onshore research storage, the first in situ testing site of CO₂ injection in Germany located near the city of Ketzin.

We used petrophysical methods that can provide the required data in a reasonable amount of time while still being representative of the in situ injection process. For two phase transport properties, we used the centrifuge technique. For resistivity measurements, we used the Fast Resistivity Index Measurement (FRIM) method in drainage and imbibition, at ambient and storage conditions. For caprock characterization, we used a fast NMR (Nuclear Magnetic Resonance) deuterium tracer technique to measure diffusivity and a modified steady state innovative technique to determine permeability. Entry pressure has also been evaluated using several methods. Resistivity and NMR logs were analyzed to provide a continuous estimation of irreducible saturation for the entire storage zone and to judge on the representativity of the samples analyzed in the laboratory.

For the Ketzin site, the storage zone is a clayey sandstone of fluvial origin locally highly cemented, with porosity around 30% and permeability ranging from 100 to 300 mD. Two zones were identified on the logs characterized by two different irreducible saturation ranging from 15 up to 35%. The measured relative permeability curves show a sharp decrease of the water effective permeability and suggest that a saturation lower than 50% cannot be reached in practice. The exponent of the resistivity index curve is about 1.7, lower than the default value of 2. The caprock has a permeability of 27 nD, a porosity around 15% and a pore diffusivity of $0.8 \times 10^{-9} \text{ m}^2/\text{s}$.

INTRODUCTION

Carbon Capture and Sequestration (CCS) is one of the many solutions to limit the current emissions of carbon dioxide into the atmosphere resulting in global warming. Although depleted oil and gas reservoirs can be used for CCS, their worldwide capacity and distribution is much less attracting than saline aquifers. From the petrophysical point of view, quick appraisal of such formation must be performed with appropriate laboratory experiments. The experimental methods are similar to those applied to oil and gas reservoirs but for CCS, the first drainage is a key process which is not of primary interest when producing gas. In addition, specific protocols are needed to characterize caprock samples.

The study was conducted in the framework of the COSMOS-2 program linked to the Ketzin EU-project CO₂SINK, which represents the first onshore *in situ* testing site of carbon dioxide (CO₂) injection in Europe (Schilling *et al.*, 2009). The Ketzin project is located at the Ketzin anticline, which is located approximately 25 km west of Berlin (Förster *et al.*, 2006). Target reservoir is the saline aquifer of the Triassic Stuttgart Formation at a depth of 625 to 700 m at the injection site. Three boreholes were drilled, including coring of the target reservoir, and instrumented

in 2007 to realize injection (CO₂ Ktzi 201/2007 borehole) and monitoring of CO₂ (CO₂ Ktzi 200/2007 and CO₂ Ktzi 202/2007 boreholes; Prevedel *et al.*, 2008). Since June 2008, 53 000 t of CO₂ (September 2011) has been injected and continuously monitored (Wüerdemann *et al.*, 2010; Martens *et al.*, 2011). For monitoring of CO₂, the injection well and the two observation wells were equipped with geophysical sensors including *e.g.* a fiber-optic-sensor cable loop for Distributed Temperature Sensing (DTS; all wells) and a Vertical Electrical Resistivity Array (VERA) consisting of fifteen toroidal steel electrodes per well and 15-line surface connection cables (Prevedel *et al.*, 2009; Giese *et al.*, 2009). In recent studies, Electrical Resistivity Tomography (ERT) based on cross-hole measurements has been evaluated as a suitable method to detect the resistivity changes caused by CO₂ injection and migration in geological reservoirs (Ramirez *et al.*, 2003; Christensen *et al.*, 2006).

Both, reservoir simulations and the application of resistivity monitoring techniques require petrophysical data, beside geological information and appropriate up-scaling methods. In this study, we conducted not only a series of experiments to fulfill these requirements, we suggest also a best-practice workflow to ensure the usefulness and the coherency of the data obtained. A first storage capacity evaluation can be made from porosity

and irreducible saturation, among other parameters, and they can be estimated from log and laboratory data. More precise evaluation can be performed from numerical simulations of CO₂ injection where at least, permeability, capillary pressure and water relative permeability must be known. Furthermore, in the present context, resistivity data acquired are closely related to the new *in situ* monitoring technology (VERA system), which has been developed and tested in other research programs (Kiessling *et al.*, 2010; Bergmann *et al.*, 2010).

In this study, the samples analyzed are from the cored reservoir and caprock section of the Ketzin 201 borehole. Some experiments conducted are often part of a standard characterization scheme (like mercury injection), others are much more advanced (like centrifuge relative permeability or resistivity measurements at *in situ* conditions) but all must be carefully planned in terms of core preparation and handling to insure coherency. Some techniques presented here could also be used as a screening method before going to more sophisticated and time consuming experiments performed with supercritical CO₂ at storage conditions. For example, the centrifuge technique is a very efficient screening method to evaluate simultaneously capillary pressure and water relative permeability curves on several samples in a single run. In this work, we also show how caprock formation could be characterized in terms of permeability, entry pressure and diffusivity using new and optimized techniques. On the Ketzin site, published petrophysical studies focused on the effect of CO₂ on permeability, resistivity and *P*-wave velocity (Zemke *et al.*, 2010) and the effect of CO₂ containing impurities (such as SO₂, Kummerow and Spangenberg, 2011) on these properties. Both studies concluded that (pure) CO₂ injection has little impact on the above mentioned properties when monitored over long periods of time (up to 1 year). However, in the presence of SO₂, this is not the case and the pore structure is modified, as shown by NMR measurements, generating fine migration, permeability and *P*-wave velocity changes.

After an overview on the applied petrophysical methods, we present the results of the Ketzin analysis from log to laboratory scale, showing the measured reservoir (transport) and caprock properties as integrated concept.

1 PETROPHYSICAL METHODS

Several laboratory techniques were applied for characterizing pore structures, for the evaluation of transport properties of reservoir rocks and for the assessment of

caprock properties. We present here the workflow of the measurements conducted in this study, starting from sampling and petrophysical standard methods to more advanced experimental settings.

1.1 CT Scan Characterization, Sample Selection, and Sample Preparation

Prior to plugging, full-size cores were analyzed using a medical X-ray CT scanner to detect major heterogeneities and perform the plugging in favorable zones. For sensitive samples of the caprock zone, it was necessary to saw a cube shaped sample first. This sample was then machined very carefully obtaining a cylinder fitting the core holder. Since porosity was measured using NMR techniques described below, samples were never dried but simply flushed with synthetic brine, except before mercury injection experiments; in that case, the drying is performed at 60 °C until a stable weight was reached.

1.2 Pore Entry Size Distribution by Mercury Injection

High Pressure Mercury Injection (HPMI) capillary pressure experiments were performed on trim ends after coring the plugs from the full size samples. In a mercury injection experiment, one measures the volume of mercury penetrating the porous media for a given pressure (see *e.g.* Dullien, 1992). From the derivative of that curve, one can obtain the pore throat distribution $f(d_{HG})$ according to:

$$f(d_{HG}) = \frac{P^2}{2\gamma \cos \vartheta} \frac{dS}{dP} \quad (1)$$

where P is pressure, S saturation, γ surface tension and ϑ contact angle. Here, the function f is a true distribution in the mathematical sense. However, it is well known that f is not the appropriate way for representing the throat distribution (Lenormand, 2003). Therefore, the dimensionless function g defined by:

$$g(d_{HG}) = P \frac{dS}{dP} \quad (2)$$

is plotted in order to retrieve the “usual” aspect of HPMI derived distribution. The derivative is calculated using spline fitting of the $S(P)$ curve.

1.3 NMR T₂ Distribution

NMR measurements were performed using two low-field instruments (*Oxford Instruments*) operating at 2 MHz for plugs with a diameter of 40 mm and 23 MHz for plugs with a diameter of 15 mm, the latter used to

perform diffusion measurements. NMR porosity and T_2 relaxation time distributions, calculated using an in-house software, were measured on all plugs without drying. First, NMR was used for determination of pore volumes after coring from the full-size core and re-saturation by flooding. The pore volume was deduced from the total NMR magnetization after calibration with a known volume of water. Porosity was calculated from the pore volume and the total sample volume given by the diameter D (40 mm) and the length L (25 or 30 mm) of the sample. Second, NMR was used as an indicator of pore-size distribution, in complement to the pore entry size distribution determined by mercury injection. The measured T_2 distribution is related to the distribution of the volume-to-surface ratio of a pore, called the pore-size distribution, by the equation:

$$\frac{V}{S} = \rho_2 \left(\frac{1}{T_2} - \frac{1}{T_{2B}} \right)^{-1} \quad (3)$$

where ρ_2 is a surface relaxivity, V and S is the volume and surface of a pore, respectively, and T_{2B} represents the bulk water relaxation (about 3 s at 30 °C). Based on our experience (Fleury, 2007), an order of magnitude of 5 $\mu\text{m/s}$ should be chosen in the present case, much lower than the value taken by Zemke *et al.* (2010) (50 $\mu\text{m/s}$). Typically, a relaxation time of 10 ms corresponds to a V/S ratio of 10 nm but this approximate correspondence has no impact in our study. Water relaxations in small pores from the clays are typically below 5 to 10 ms, depending on the type of clay.

NMR cut-off measurements were also determined using centrifuge de-saturated plugs. If Sw_{irr} is the smallest saturation obtained at the highest capillary pressure (2.2 bar) on a given sample (asymptotic saturation value on the P_c curve), the cut-off value T_{2c} is determined using the T_2 distribution measured on the same sample saturated at 100% and is defined as:

$$\int_0^{T_{2c}} A(T_2) dT_2 = Sw_{irr} \quad (4)$$

where $A(T_2)$ is the relaxation-time distribution. Relaxation times up to the cut-off T_{2c} corresponds to small pores that are not de-saturated.

1.4 Formation Factor and Resistivity Index Measurements

The formation factor was measured simultaneously with permeability using a classical face to face two electrode system at ambient laboratory temperature. The conductivity of the brine was measured at the outlet of the core

holder using a conductivity meter in which a temperature sensor was included. The formation factor was then determined from the ratio of brine to sample conductivity ($FF = C_w/C_0$) measured at the same temperature. The sample conductivity C_0 was determined using the measured resistance R , the sample length L and diameter D by the formula $C_0 = L/(R \pi D^2/4)$.

The method used to measure resistivity index (RI) is based on the Fast Resistivity Index Measurement method called FRIM (Fleury, 1998). It was originally planned to use a screening method (Han *et al.*, 2007) but the Ketzin sample consolidation was not sufficient for this technique to be applied. At ambient conditions, we measured resistivity indexes in drainage and spontaneous imbibition using the system presented in Figure 1. In drainage, the pressure difference between air and brine is increased step-wise (typically using pressure differences of 50, 100, 180, 360, 640, 1 300, 1 800 mbar) to decrease the saturation, and then decreased again in imbibition. From the recording of the average water saturation (Sw) using the water level detector (water expelled from the sample), and the average resistance using the impedance meter, we can deduce “continuous” $RI-Sw$ curves. Compared to other systems, this experiment has very little sensitivity to saturation profiles, if any, contrary to flooding experiments with electrodes located along the sample. At storage conditions, the measurement principle is similar to the one described above but the experimental set-up is designed to handle high pressure and temperature (Fleury, 2003), as well as CO_2 at typically 100 bar. In the performed study, the average pore pressure was 80 bar, the confining pressure

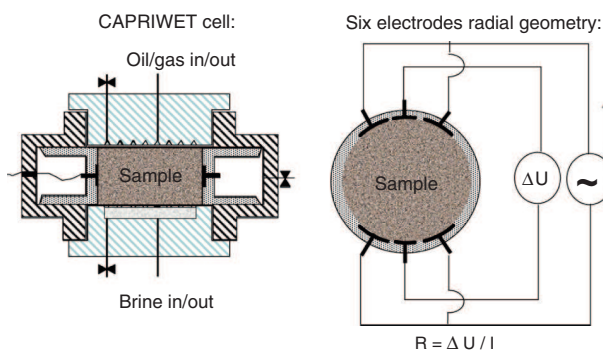


Figure 1

Schematic of the cell and electrode geometry for measuring resistivity index. A water wet ceramic located at the bottom of the sample prevents the breakthrough of oil or gas at the lower face of the sample and allows reaching high capillary pressure uniformly along the sample. The brine outlet is connected to a level detector to determine brine saturation. Sample length is 25 mm.

110 bar and the temperature 30 °C. The length of the sample used is 25 mm (diameter = 40 mm).

At ambient conditions, in addition to the standard 1 kHz frequency measurement, the system allows scanning the frequency range [1 Hz-1 MHz] using an advanced impedance meter (Fleury and Liu, 2000). In this case, it was of interest to study the low frequency ranges around 1 Hz, because it is close to those used in the measurement cycles of the VERA monitoring system installed in Ketzin (Schmidt-Hattenberger *et al.*, 2011a). The frequency dispersion was studied and we concluded that resistivity index data obtained at 1 kHz can be used at 1 Hz without significant deviation. This is not presented in this paper.

1.5 Centrifuge Capillary Pressure and Relative Permeability Measurements

We performed air-brine first drainage centrifuge capillary pressure and relative permeability measurements using an automated centrifuge (Fleury *et al.*, 1998). Essentially, the system can record continuously the amount of water expelled from the sample as a function of time and speed of rotation. When the saturation in the sample is stabilized, the equilibrium between capillary and gravity forces is given by (Fig. 2):

$$P_C(R) = \frac{1}{2} \omega^2 (R_{\max}^2 - R^2) (\rho_w - \rho_g) \quad (5)$$

where ω is the rotation velocity, R_{\max} is the distance between the rotation center and the outlet face of the

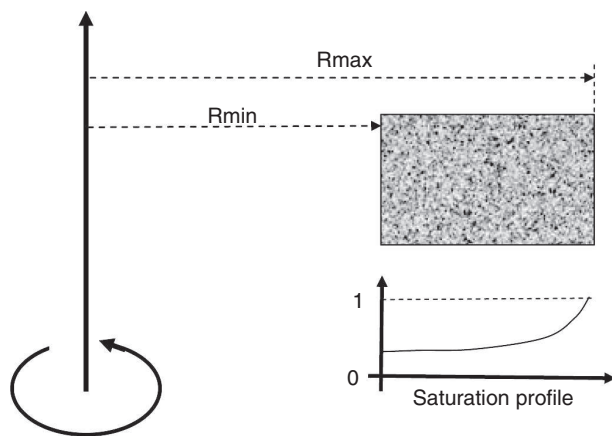


Figure 2

Schematic of the centrifuge experiment. In the set-up used, $R_{\max} = 20.4$ cm and R_{\min} is given by the length L of the sample $R_{\min} = R_{\max} - L$ ($L < 6$ cm). The centrifuge rotation speed ranges from 200 up to 4 500 rpm. In the present experiments, the largest speed of rotation was 2 200 rpm.

plug, ρ_w and ρ_g are the densities of brine and air. According to the above equation, the maximum pressure P_c is obtained at the inlet face of the plug (R_{\min}), then it diminishes to zero at the opposite face (R_{\max}), which stays at 100% saturation. As a result, there is a saturation profile and a non-trivial calculation is necessary. We used the Forbes method (Forbes, 1991) to calculate capillary pressure curves from average saturation data. The number of points describing the P_c curves is directly related to the number of speed steps.

With the recording of water saturation *versus* time and speed of rotation, the water relative permeability curve can be deduced. Indeed, the time needed to go from one equilibrium state to another (one speed of rotation to another) is directly linked to the effective permeability of one phase (brine) in the presence of the other one (air). Again, due to the saturation profile, a numerical interpretation is necessary. It consists of fitting the recorded saturation data using a forward model based on two-phase Darcy's law in a centrifuge with appropriate boundary conditions. We used the SENDRA software (from *Weatherford*[®]) to perform this analysis.

The centrifuge experiment, when performed with continuous recording of saturation, is well adapted for the simultaneous determination of air-brine P_c and K_r curves in the entire saturation range (Fig. 3). It can be performed on small samples ($L = 30$ mm, $D = 40$ mm), which was a constraint in the present situation. Although it is a well known technique among experts in the field of petrophysics, it is not routinely performed despite many advantages. First, there are technical difficulties of measuring the water saturation while rotating and second, the numerical interpretation needs a specific procedure described elsewhere (Bauget *et al.*, 2012). The great advantage of centrifuge air-brine K_r experiments compared to standard gas injection is that it is not subjected to fingering instabilities induced by local heterogeneities. In a gas injection experiment, this is the case and the saturation ranges that can be explored are limited and a function of the length and permeability of the core. Furthermore, a numerical interpretation is also required contrary to common practices (*e.g.* Bennion and Bachu, 2008), in which the knowledge of the P_c curve is necessary, implying another experiment to be ideally performed on the same sample. The drawback is that the centrifuge experiment is difficult to perform at storage conditions and that the gas relative permeability cannot be obtained. However, due to the low viscosity of air (and hence its very high mobility compared to water), the dynamics of the system is dominated by brine. In the inversion process described above, it was indeed observed that the gas relative permeability curve (K_{rg}) that needs to be given in the simulation has no influence

on the result, as expected. To some degree, this is also the case for field simulations. Hence, we obtained from this experiment the most important parameter, the water Kr curve, and in the absence of Krg data for the considered storage, one can take an arbitrary shape based on literature data.

At the end of drainage, samples are immersed in water in order to obtain the residual gas saturation. Prior to centrifugation, brine permeability and formation factor are measured. For various reasons (corrosion, salt precipitation), a diluted formation brine (50 g/L) has been used but this has no consequences on the transport properties determined in the centrifuge experiment. Although

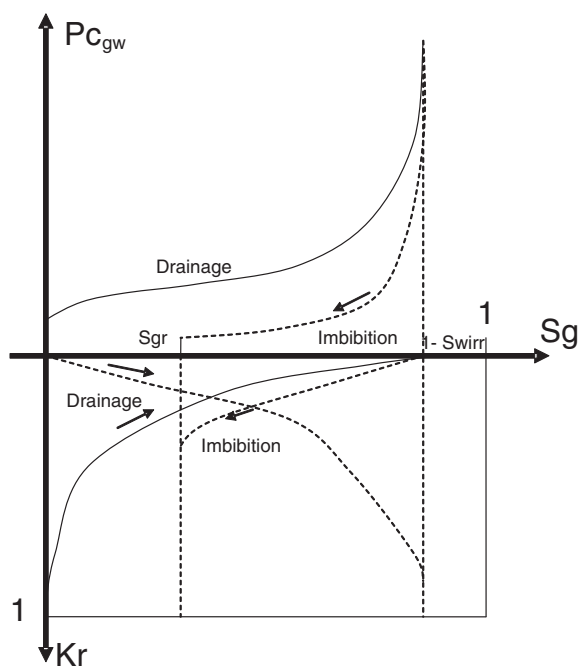


Figure 3

Schematic of drainage and imbibition gas-water capillary pressure (P_c) and relative permeability (Kr). The centrifuge experiment allows determining simultaneously the drainage P_c curve and water relative permeability curve, in the largest saturation range possible.

the system can handle sample lengths of up to 60 mm, we used a sample of length 25 mm or 30 mm ($D = 40$ mm) in order to improve the accuracy at low capillary pressures. The accuracy of volume measurements is 0.05 cc, about 1% of the pore volume.

1.6 Caprock Permeability Measurements

Both the steady state and pulse decay methods were used. In the steady state method, a pressure gradient is applied and the corresponding water flux is measured. The water permeability k (m^2) is deduced from Darcy's law:

$$Q = S \cdot \frac{k}{\mu} \cdot \frac{P_u - P_d}{L} \quad (6)$$

where Q is the water flux (m^3/s), S the sample surface (m^2), μ the water viscosity (Pa.s), L the sample length (m), P_u the upstream pressure (Pa) and P_d the downstream pressure (Pa). The experimental set-up included two pistons (A and B in Fig. 4). Piston A maintains the upstream pressure. Downstream pressure, maintained by piston B, was chosen to be lower than P_u , in order to create a flow of water from A to B. Displacements of pistons A and B provide measurements of the water flux Q (push-pull mode) using high precision pumps.

Upstream and downstream pressures were maintained independently by each piston. Upstream pressure was set to 7.5, 8 and 8.5 MPa, and corresponding downstream pressure was set respectively to 6.5, 6 and 5.5 MPa in such a way that the pore pressure was maintained at a mean value of 7 MPa, and the pressure gradient was set to 1, 2 and 3 MPa (each pressure gradient lasted three hours). For the Ketzin study, the confining pressure was set to 17 MPa, reproducing *in situ* stress conditions occurring at ~ 700 m depth (Zemke *et al.*, 2010)

The pulse decay method (Brace *et al.*, 1968) is applicable to a sample bounded by two reservoirs initially at equal pressure but here, it was applied with water. A pressure rise is suddenly imposed in the upstream

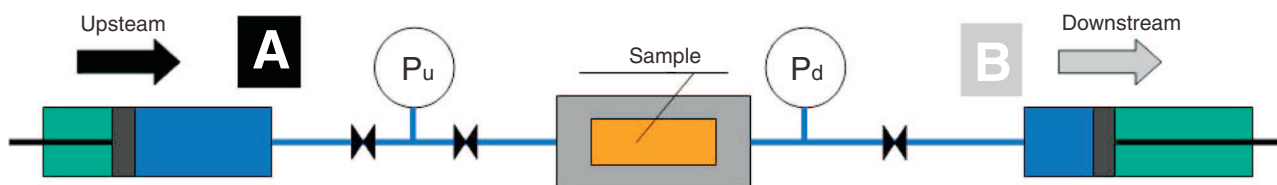


Figure 4

Simplified diagram of the experimental set-up. A and B represent the two pistons of the high precision pumps used upstream and downstream. The assembly is placed in an oven in which the temperature is regulated within 0.2 °C.

reservoir and the pressure evolution is recorded in both reservoirs. The determination of the permeability is made using the transient phase leading to pressure equilibrium in the reservoirs. The water motion within the sample is described by the equation:

$$\frac{S_s}{\rho_w g} \frac{\partial P_w}{\partial t} = -\nabla \cdot \left(\frac{k_w}{\mu_w} \cdot \nabla P_w \right) \quad (7)$$

where S_s (m^{-1}) is the specific storage of the sample and corresponds to the volume of water over the total volume of the rock which can be stored per unit of water head change. Both permeability and specific storage can be obtained when interpreting a single pulse decay experiment.

1.7 Caprock Entry Pressure Measurements

Two measurement techniques were used. First, the standard method (Li *et al.*, 2005) in which an upstream gas pressure is increased step by step until water is displaced at the outlet. The duration of the respective steps should be long enough to allow for observation of downstream water production (3 to 4 days). The water production itself is recorded by a pump placed downstream. The second method follows the dynamic approach presented by Egermann *et al.* (2006). Here, gas is injected upstream at a constant pressure P_g , gas pressure is chosen above the entry pressure. Upstream, gas displaces water until gas is in contact with the sample's surface. As the downstream pressure is maintained to be constant, two different flow rates are observed: before and after gas entry. The flow rate difference is related to the entry pressure value. Before conducting the caprock entry-pressure experiments, the permeability was measured using the steady state method (three flow rates at three different pressure gradients, see previous paragraph).

1.8 Caprock NMR Diffusion Measurements

A deuterium tracer technique was used to measure the water diffusivity in the pore space (Fleury *et al.*, 2009; Berne *et al.*, 2010), instead of the more conventional PFG-NMR self-diffusion technique which is very difficult to apply due the short life time of the magnetization. Essentially, a small sample (*e.g.* a cylinder, 15 mm in diameter and length) initially saturated with brine is immersed in deuterium (D_2O , purity 99.5%, Fig. 5). Because D_2O (2H) has a very different resonance frequency (in our case 3.6 MHz instead of 23.7 MHz) and is therefore not measured, we can measure a 1H water concentration inside the sample as a function of time

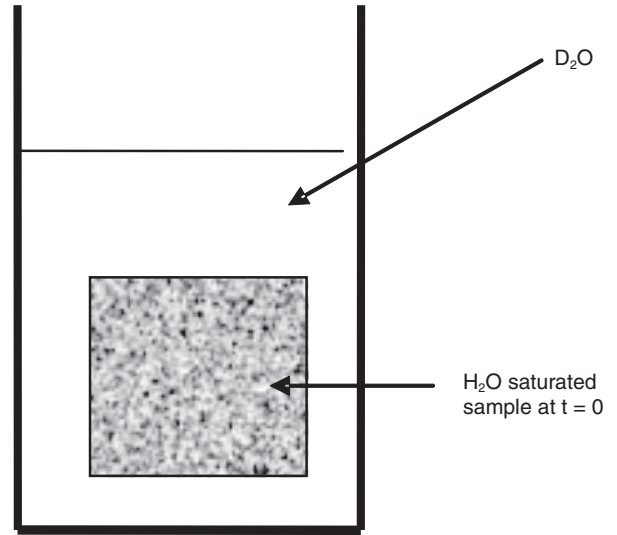


Figure 5

Schematic of the deuterium NMR diffusion experiment on a caprock sample.

by simply recording the magnetization as a function of time. This magnetization also contains the signal from water outside the sample. However, this water has a very long relaxation time compared to those inside the sample (4 s compared to 10 ms) and therefore can be removed easily in the distribution. Moreover, since this water is also strongly under-polarized due to a short repetition delay time (1 s), this correction is small. Then the magnetization $M(t)$ is analyzed using analytical expression of a fluid diffusing out of a cylinder:

$$\begin{aligned} C^* &= \frac{C-C_f}{C_i-C_f} = \frac{M-M_f}{M_i-M_f} = C_{ps} C_{cyl} \\ C_{ps} &= \sum_{n=0}^{\infty} \frac{2\alpha(1+\alpha)}{1+\alpha+\alpha^2 q_n^2} \exp\left(-D_p q_n^2 \frac{t}{r^2}\right) \\ C_{cyl} &= \sum_{n=0}^{\infty} \frac{4\alpha(1+\alpha)}{4+4\alpha+\alpha^2 q_n^2} \exp\left(-D_p q_n^2 \frac{t}{r^2}\right) \end{aligned} \quad (8)$$

where q_n are the non-zero positive roots of:

$$\alpha q_n J_0(q_n) - 2J_1(q_n) = 0 \quad (9)$$

J_i is the Bessel function of the first kind of order i , r is the radius of the cylinder, $2l$ the length of the cylinder, and α is the volume ratio of deuterium to water ($\alpha = 10$ in our situation). Since concentration is proportional to magnetization, the concentration C^* is directly obtained from M , M_i (initial value) and M_f (final value), without calibration. The pore diffusivity D_p is obtained by fitting the curve $C^*(t)$ using Matlab routines.

2 RESULTS

2.1 Log Data Analysis

As part of the wireline-logging program of the CO₂ Ktzi 201/2007 borehole, NMR data were recorded in addition to the performed standard logging measurements of the natural radioactivity (GR-log), acoustic properties, electrical resistivity, bulk density and neutron porosity. The entire log data suite has been analyzed to derive lithological and petrophysical information, calibrated on core data (Norden *et al.*, 2010). In this paper, we focus on the interpretation of the NMR and resistivity data of the injection interval (632 to 652 m) and of the caprock at a short distance above the injection interval (620 to 632 m), where samples of this study were analyzed.

The Stuttgart Formation, which was completely cored at the CO₂ Ktzi 201/2007 borehole, is lithologically heterogeneous, consisting of sandstone, siltstone, and mudstone intervals, the latter inter-bedded with variable

amounts of anhydrite and minor coal (Norden *et al.*, 2010). The sandstones are of fluvial origin and show remarkable differences in porosity, ranging from 13% to 26%. In areas, where the sandstone is intensely cemented by anhydrite and analcime, nearly no porosity is present. The dominantly fine-grained and well to moderately-well sorted, immature sandstones classify as feldspathic litharenites and lithic arkoses (Förster *et al.*, 2010): Quartz (22-43 wt%), plagioclase (19-32 wt%) and K-feldspar (5-13 wt%) predominate mineralogically. Muscovite plus illite and mixed-layer minerals are omnipresent (4-13 wt%). The depth interval studied (632-652 m, Fig. 6) hosts the main-reservoir sandstone and represents the upper part of the total Stuttgart Formation (630-701 m). The silty to muddy rocks on top of the sandstone sequence reflect sediments of the floodplain facies, whereas the sandstone complex belongs to a fluvial channel system. In certain depth zones, the sandstone which shows often a pronounced mud-cake (indicating high porosity and permeability)

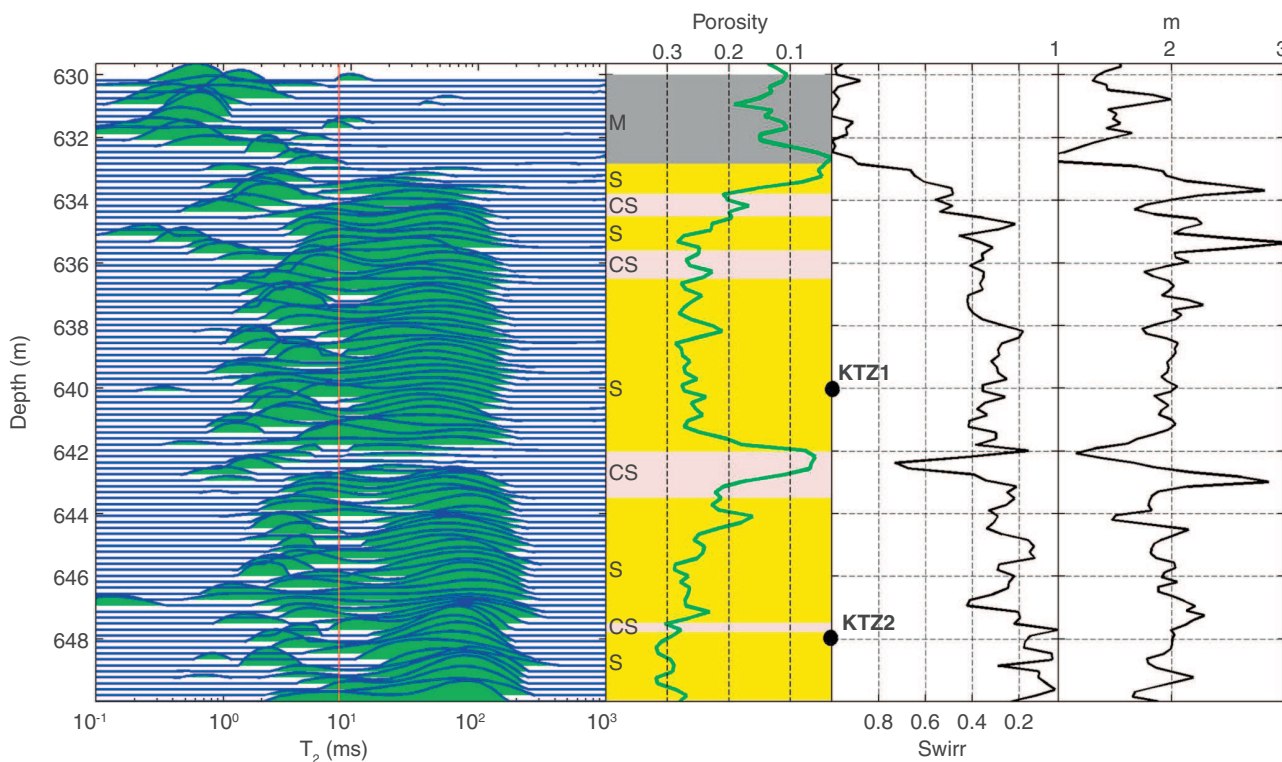


Figure 6

NMR and micro-resistivity analysis. The irreducible water saturation Sw_{irr} is deduced from the NMR T_2 distribution using a cut-off of 8 ms. The cementation exponent m is calculated from the resistivity track and NMR porosity using the measured mud filtrate resistivity. The big circles indicate the location of the samples. A simplified lithology is indicated as S for sandstone, CS for cemented sandstone and M for mudstone.

is strongly cemented, perhaps indicating different merged channel systems (Förster *et al.*, 2010). The caprock interval cored and analyzed in this study consists of couplets of mudstone with anhydrite or dolomite beds of the Triassic Stuttgart and Weser Formations (Fig. 7), which represent sediments of mud-sulfate playa facies (Beutler and Nitsch, 2005).

Raw NMR magnetization decay data and resistivity data were extracted from the recorded logging data file provided by the logging company. For NMR, we computed the T_2 distribution using an in-house software, which was also used for analyzing laboratory data. Unlike the NMR distribution presented by Norden *et al.* (2010), no data averaging is performed in order to have a better vertical resolution. Therefore, the distribution is shown at the highest possible vertical resolution (about 0.25 m). For resistivity, we extracted the micro-resistivity track (MCFL track), for which the depth of measurement is a few inches, which is similar to the NMR investigation depth. Hence, due to the high permeability in the injection interval, this resistivity track is clearly reading in the invaded zone. Taking this as a prerequisite, the formation brine resistivity is not needed in the interpretation and one can take the known mud-filtrate resistivity instead. The cementation

exponent m of the Archie relationship was calculated using the formulae:

$$m = -\frac{\log (FF)}{\log (\Phi_{NMR})} \text{ where } FF = \frac{Rt}{R_w}(1 + 0.785R_w) \quad (10)$$

Rt is the resistivity given by the logging tool (MCFL track) as a function of depth, Φ is the (total) porosity obtained by NMR, and R_w is the brine resistivity saturating the formation at the depth of measurement. The formulae for the calculation of the formation factor FF is due to clay effects and is presented in section electrical properties. As mentioned above, we take the resistivity value of the mud filtrate, *i.e.* we assumed that the near wellbore region is completely flushed by the mud filtrate. For the mud filtrate resistivity, we used the measured value ($R_w = 0.137 \Omega m$ at 20.9 °C) and the estimated formation temperature (35 °C), yielding a value $R_w = 0.103 \Omega m$ (note that the temperature correction has a significant effect on the calculation of m). Such interpretation cannot be applied in the caprock zone because no or very little invasion is occurring. Similarly, this interpretation may not be valid in the thin cemented sandstone layer present in the middle of the reservoir section, as discussed below.

The investigated reservoir section can be subdivided into two zones (upper and lower corresponding respectively to sample KTZ1 and KTZ2) separated by a cemented sandstone layer, showing very low porosities (at 642 m, Fig. 6). The upper zone is slightly less porous than the lower zone, the latter being characterized by T_2 value slightly larger. There is also a qualitative agreement between laboratory and log T_2 relaxation time distribution in terms of shape and peak positions.

The NMR data allows not only the measurement of porosity but also the determination of the irreducible saturation S_{wirr} as defined in Figure 3. Beside permeability estimation, this is the main use of relaxation time distribution. It is a direct interpretation based on the fact that the relaxation time T_2 is an indicator of pore size, as explained in the previous section. When the sample is desaturated and the capillary pressure curve (shown later) tends to an asymptotic value above 1 bar, only the largest pores are desaturated and a cut-off can be calculated from Equation (4). We found an average value of 8 ms (Fig. 7, minimum 5 ms and maximum 9 ms) when using the centrifuge experimental results. Such value is a typical cut-off value for separating water trapped in clay from inter-granular water. Note here that the usual cut-off of 33 ms applied in sandstones is inappropriate.

When local calibrations are performed, laboratory and log data agree reasonably well, but not perfectly, as shown in Table 1. Log data tends to give larger S_{wirr} values around 35% for the upper zone, and smaller

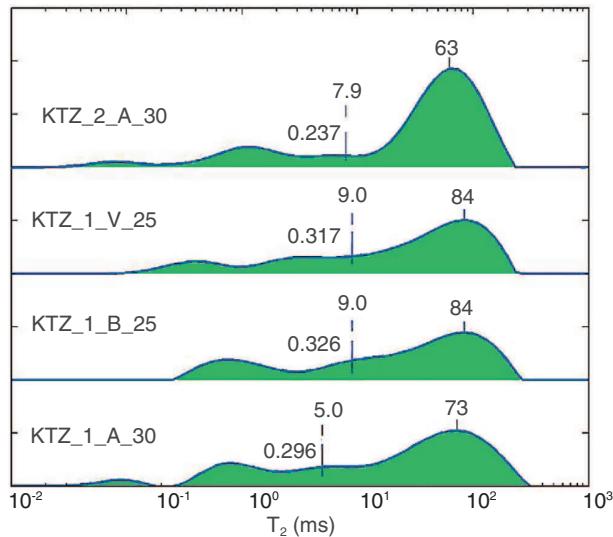


Figure 7

NMR pore size distribution measured on different plugs from the upper and lower zones. Numbers indicate the T_2 cut-off and the saturation measured after centrifugation. An average value of 8 ms has been chosen for the cut-off in the NMR log interpretation.

TABLE 1
Main characteristics of the samples from the storage zone

Sample	Depth (m)	Porosity (%)		Permeability (mD)	m		Sw_{irr} (%)	
		Lab.	log		Lab.	log	Lab.	log
KTZ 1	639.7	26.8-28.0	28	182-280	1.83-1.93	1.95	30-32	35
KTZ 2	648.9	31.4	30	104	1.92	2.01	24	15-20

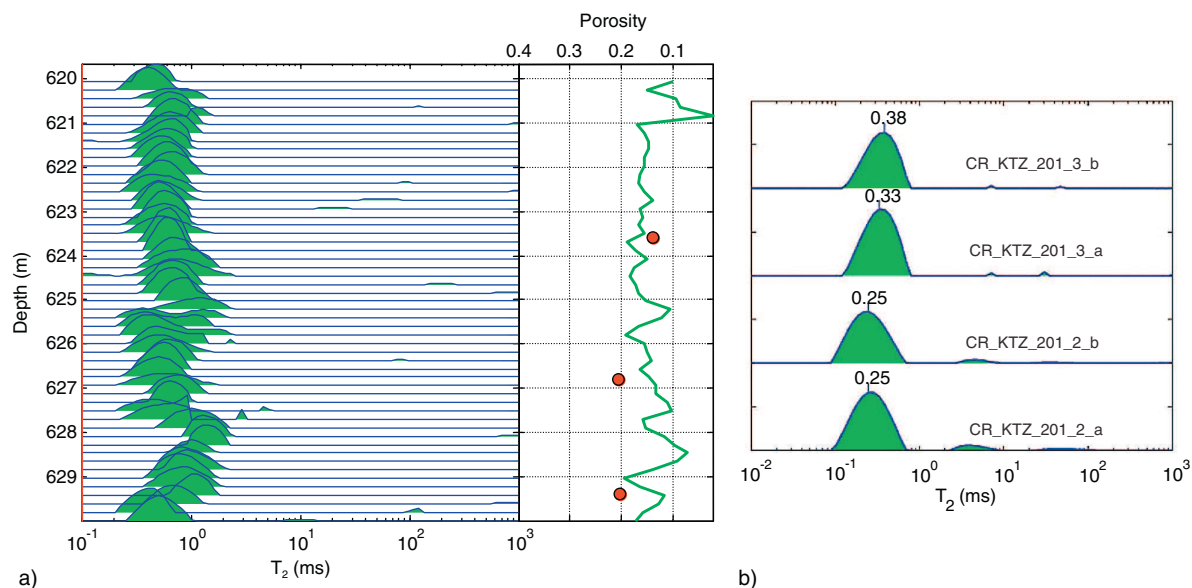


Figure 8

a) NMR data for the caprock zone immediately above the storage. Circles indicate NMR porosity measured on small samples.
b) Relaxation time distributions measured on samples in the laboratory.

values below 20% for the lower zone. There is a better agreement for the cementation values m because resistivity is much less dependant on small scales fluctuations.

For the caprock zone, the log data are plotted over an interval of 10 m above the storage (*Fig. 8*, note that the transition reservoir/caprock is at 633 m, see *Fig. 6*). The very small pore sizes characterizing the caprock formation is clearly evidenced by relaxation times around 0.5 ms instead of 80 ms. The NMR log porosity is found around 15%, a usual value for compacted formation dominated by clays. Although the small relaxation time is at the limit of resolution of the logging tool (around 0.2 ms), log porosity does not appear to be underestimated; laboratory NMR measurements show similar relaxation times, without the presence of shorter components (the resolution of laboratory measurements is about 0.08 ms).

2.2 Results: Pore Structure Characterization

From standard mercury injection experiments, we obtain the pore size distribution (*Fig. 9*). For the storage zone, the distribution of pore-entry size is narrow, with a tail toward small values representing the clays. The upper zone has the lowest porosity, highest permeability and smaller pore sizes (*Fig. 9, Tab. 1*), giving an illustration of the influence of the clays in these sandstones. The upper and lower zones also differ by a different organization of the clays in the grains, at least for the analyzed samples, as revealed by CT-scan images (*Fig. 10*). Clays are clearly laminated for the samples of the lower zone, whereas they are more dispersed for the samples of the upper zone. We will see later that the petrophysical properties measured on the upper and lower samples have differences that are linked to these observations.

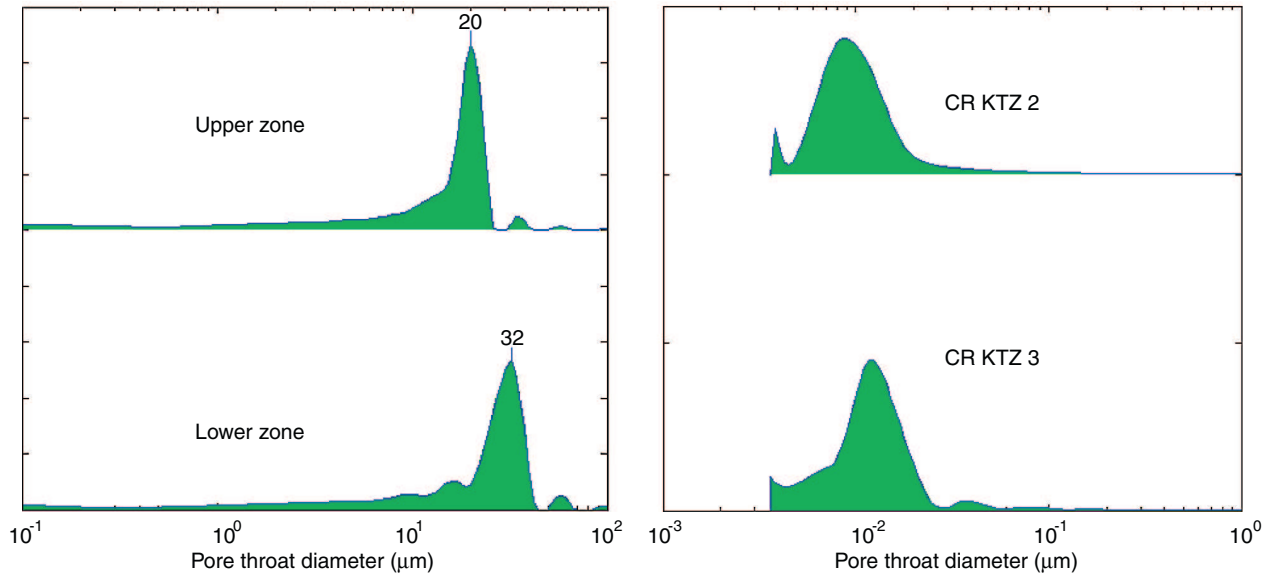


Figure 9

a) Pore size distribution obtained from High Pressure Mercury injection experiments for the storage, b) and caprock zone.

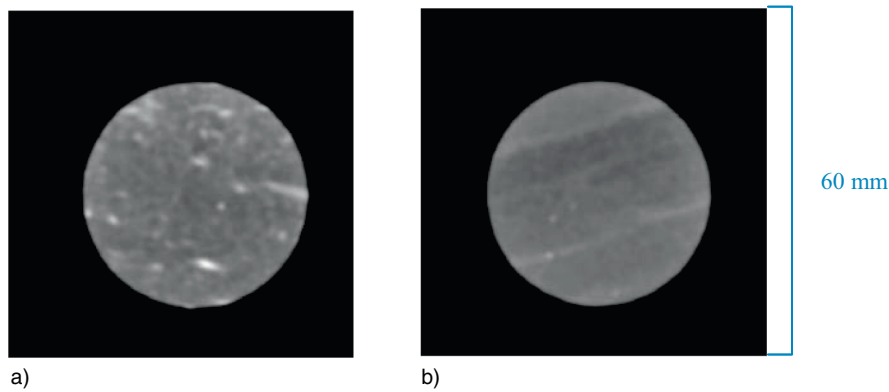


Figure 10

a) CT-scan cross sections of a plug from the upper zone, b) and a plug from the lower zone. Two different structures (laminated, dispersed) are clearly visible.

2.3 Results: Capillary Pressure and Relative Permeability, Residual Gas

We observe two groups of capillary-pressure curves (Fig. 11), which may correspond to the lower and upper zones of the reservoir, respectively. The upper zone samples, less porous and more permeable, present a slightly higher entry pressure (> 100 mbar) and a higher irreducible water saturation (about 30%, Tab. 1) while the lower zone sample, has an entry pressure less than 100 mbar and an irreducible water saturation about

24%, as already discussed in Section 2.2. The P_c curves determined during the resistivity experiments described later are identical (not shown). The measured residual gas saturation (S_{gr} , Tab. 2) are small (0.1 to 0.18 respectively for the upper and lower zone) and appear directly linked to the irreducible water saturation.

Using the SENDRA software, we simulated the air/brine primary drainage centrifuge experiment for the four samples. In order to reproduce the measured brine productions, capillary pressure and relative permeability curves were adjusted through a two step optimization

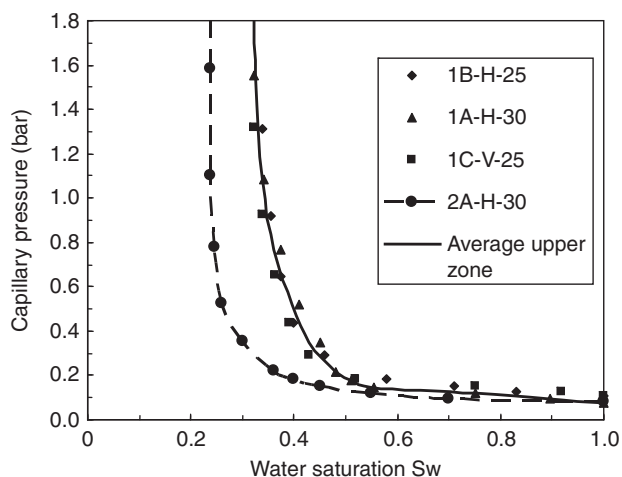


Figure 11

Capillary pressure curves obtained from the centrifuge experiment. For the upper zone, the curves measured on 3 samples (1A, 1B and 1C) were averaged into one single curve. For the lower zone, only one sample was available (2A).

TABLE 2

Tabulated capillary pressure curves. S_{gr} is the residual gas saturation after spontaneous imbibition

Lower zone		Upper zone	
S_w	P_c (bar)	S_w	P_c
1.000	0.080	1	0.078
0.700	0.094	0.89	0.092
0.550	0.121	0.75	0.119
0.450	0.149	0.55	0.147
0.400	0.181	0.51	0.178
0.360	0.220	0.48	0.216
0.300	0.353	0.43	0.346
0.260	0.527	0.395	0.517
0.246	0.780	0.36	0.766
0.237	1.105	0.34	1.084
0.237	1.582	0.325	1.552
0.237	2.234	0.32	2.192
$S_{gr} = 0.18$		$S_{gr} = 0.105$ (max 0.11, min 0.10)	

process. First, starting from the Forbes solution for capillary pressures (Fig. 11) and using relative permeability curves simply described by Corey's equations with

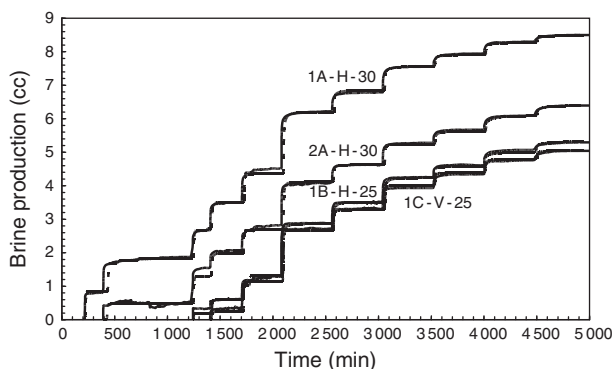


Figure 12

Comparison of measured (full line) and simulated (dashed line) water production at the end of the optimization procedure.

exponents 1, capillary pressure curves were adjusted point by point so that the simulated production matches the volume production at the end of each centrifuge speed step. This adjustment is very small and is essentially due to the different calculation of the derivative dP_c/dS_w . Then, the relative permeability (K_r) curves were adjusted in order to reproduce for each step the transient part of the production curves (Fig. 12). This adjustment is performed using automatic matching of the parameters describing the K_r curves (parameters of the LET functions given by Lomeland *et al.*, 2005). We found the following curves:

$$S_w^* = \frac{S_w - S_{wirr}}{1 - S_{wirr}} \quad (11)$$

$$k_{rw} = \frac{(S_w^*)^L}{(S_w^*)^L + E(1 - S_w^*)^T}$$

with the parameter values $L = 2.5$, $E = 45$, $T = 0.7$, $S_{wirr} = 0.285$ for the upper zone, and $L = 2.6$, $E = 10.0$, $T = 1.2$, $S_{wirr} = 0.21$ for the lower zone. This model was the best one able to reproduce the measurements. We observe two groups of water relative permeability curves, similarly to capillary pressure curves (Fig. 13), corresponding also to the two reservoir zones. For both zones, during the drainage process, water relative permeabilities decrease rapidly with water saturation. During early drainage ($S_w > 90\%$), water relative permeabilities of the upper zone samples drop rapidly by a factor of ten. Such anomalous behaviour was also observed on resistivity data described later. To situate these results using the more conventional power law model $k_{rw} \propto (S_w^*)^\alpha$ (which is however totally inappropriate here), the exponent α

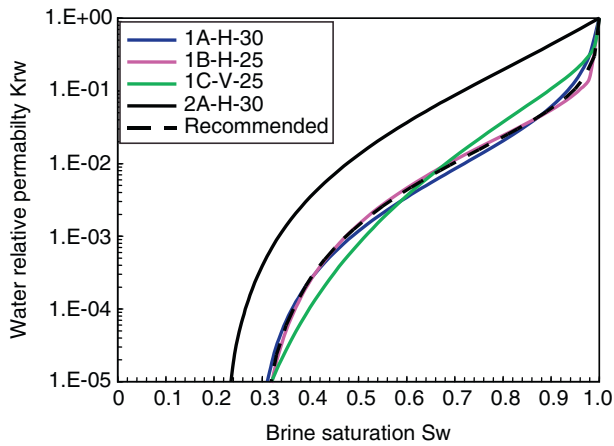


Figure 13

Water relative permeability curves described by LET functions in the full saturation range. For the upper zone (sample 1A, 1B and 1C), we recommend to the curve defined by the dashed line. For the lower zone, only one sample is available (2A).

would be around 3 in the intermediate saturation range S_w between 0.85-0.45, in agreement with the known range of values for gas-liquid first drainage (Honarpour *et al.*, 1986). For the intermediate saturations, the less permeable sample (lower zone) has the highest water relative permeability, about one order of magnitude greater than the upper zone ones. Therefore, the apparent water permeability is 3 to 5 times higher for the less permeable sample of the lower zone.

From the point of view of apparent permeabilities of the two intervals studied, the relative permeability effects can easily compensate the difference of absolute permeabilities. We observe that in the water saturation range greater than 45%, water relative permeabilities are greater than 10^{-3} - 10^{-2} meaning that the apparent water permeabilities (the product $K Kr$) will remain greater than 0.1-1mD. In such a case CO₂ injection can still be considered but it will require a growing pressure as water saturation decreases in the reservoir. Below water saturations of 45%, relative water permeabilities drop drastically; thus water mobility will become too low and further increase of CO₂ saturation will not be possible in practice; consequently, a significant part of the estimated reservoir volume will not be accessible for CO₂ storage.

2.4 Results: Electrical Properties

Investigating electrical properties at the Ketzin site plays an important role in the geophysical monitoring

concept. Field activities comprise different setups: *e.g.* cross-hole Electrical Resistivity Tomography – ERT (Schmidt-Hattenberger *et al.*, 2011b), surface-downhole ERT as well as electromagnetic surveys (Girard *et al.*, 2011; Streich *et al.*, 2011). As mentioned before, all three wells of the Ketzin pilot site were equipped with permanent electrical sensors in order to perform electrical tomography between the wells, and finally estimate the corresponding CO₂ saturation. Since the output of the *in situ* geoelectrical system is a 3D resistivity image, the desired calculation of the CO₂ saturation requires a reliable laboratory-based resistivity-saturation relationship. The essential part of this petrophysical conversion is the resistivity index-water saturation ($RI-S_w$) relationship, ideally based on experiments at reservoir conditions in order to obtain representative results, as clearly highlighted by Nakatsuka *et al.* (2010).

Formation Factor

Formation factor are determined routinely. However, specific procedures are needed in clay rich systems. Indeed, due to the mineralogical structure of clays, there is a well known excess conductivity due to double layer effects. This is usually studied by decreasing the salinity of the brine and plotting the conductivity of the sample C_0 versus brine conductivity C_w (Fig. 14). Here, we used the formation brine composition with successive dilution. The excess clay conductivity is given by the intercept at $x = 0$ of the sample conductivity. The data can be fitted with the following best fit equation:

$$C_0 = 0.1119C_w + 0.0878 \text{ [S/m]} \quad (12)$$

$$R^2 = 0.999$$

Based on this relation, the formation factor can be calculated using a Waxman-Smiths model in which the above offset is taken into account:

$$FF = \frac{0.785 + C_w}{C_0} \quad (13)$$

When calculating the cementation exponent m of the Archie relationship ($m = \log(FF)/\log(\Phi)$), the values are larger by about 0.03 for the laboratory data and 0.06 for log data compared to the calculation using $FF = C_w/C_0$. This difference is due to the temperature difference between the laboratory conditions (about 20°C) and the subsurface temperature.

Resistivity Index

The resistivity index curves on a sample from the upper zone (Fig. 15) cannot be described by a simple Archie

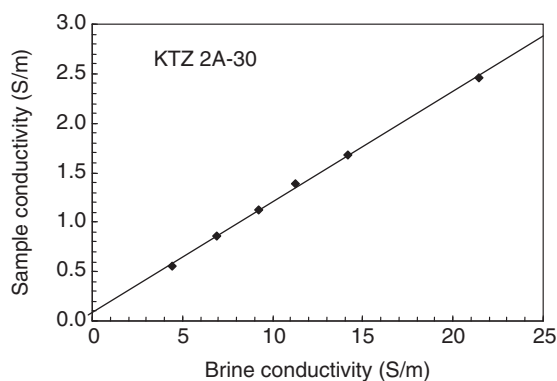


Figure 14

Sample conductivity versus brine conductivity using the formation brine composition.

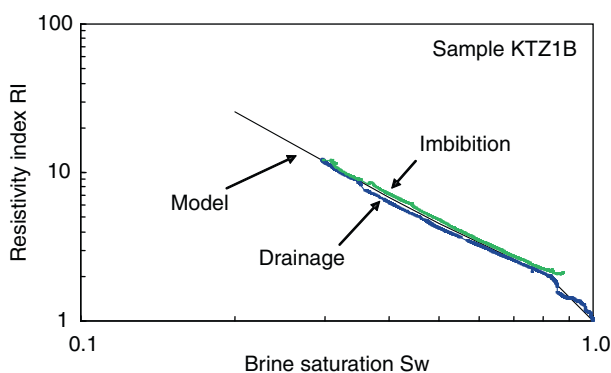


Figure 15

N_2 -brine resistivity index measured at ambient conditions for sample KTZ1 (upper zone).

law. At the beginning of drainage ($S_w^{-3.5}$), there is first a sharp increase of RI followed by a change of slope and a more classical behavior ($S_w^{-2.0}$). The model deduced from the data is the following:

$$RI = S_w^{-3.5} \quad 0.82 < S_w < 1$$

$$RI - RI_0 = S_w^{-2.0} \quad S_w < 0.82 \quad RI_0 = 0.56 \quad (14)$$

in drainage and imbibition

This means that the resistivity changes are larger at large saturation ($S_w \approx 0.8$) compared to a simple Archie law S_w^{-2} . The origin of the sharp increase at the beginning is not due to an experimental artefact (there is no dead volume correction and the RI curve is obtained directly from the data). It is also consistent with K_{rw} curves. A possible explanation is that a network of large pores may exist in the sample. This network may have a large contribution in terms of conductivity and when invaded by air, this contribution is rapidly lost. There is no hysteresis effects (no difference between drainage and imbibition) as expected for this type of porous media.

For the sample of the lower zone, a classical Archie behavior is found with a saturation exponent $n = 1.8$ for the N_2 -brine system at storage conditions (Fig. 16). At ambient conditions (a pore pressure of 8 bar), we found a similar value of the saturation exponent n (1.7), within experimental errors. However, for the CO_2 -brine system at storage conditions (Fig. 16), the saturation exponent n is significantly lowered (1.65). This behavior has been observed on sandstones in another investigation performed at IFP Energies nouvelles (Fleury *et al.*, 2010, unpublished) and therefore it is

believed not to be specific to the Ketzin samples but rather to the presence of clays and presumably in conjunction with a lower pH value caused by CO_2 dissolution. Another difference between the two systems is the much lower interfacial tension for the CO_2 case (about 28 instead of 73 mN/m). Hence, the water distribution in the pore network may not be necessarily the same, yielding a slightly different n value. Note also that the final saturation is lower ($S_w = 0.1$ instead of 0.23) due to the lower interfacial tension (a similar pressure was applied on the CO_2 experiment). A low n value (1.62) has also been found by Kummerow and Spangenberg (2011) using a very different set-up at storage conditions.

2.5 Results: Specific Measurements on Caprocks

In this section, we present the experimental results on samples from the caprock formation. Permeability and entry pressure were measured, as well as water diffusivity to provide basic data for modeling CO_2 migration, if any, at the base of the caprock.

Permeability

The displaced volume of water in the “push-pull” mode is shown in Figure 17 for both pumps A and B. At steady state, these two volumes should be equal but this is reached only after a certain time delay, of the order of 2 hours. Hence, when the evolution is linear, the slopes corresponding to the upstream and downstream water flow can be used to calculate permeability. This procedure was repeated for three successive flow rates. When the successive flow rates (Q) are plotted against the

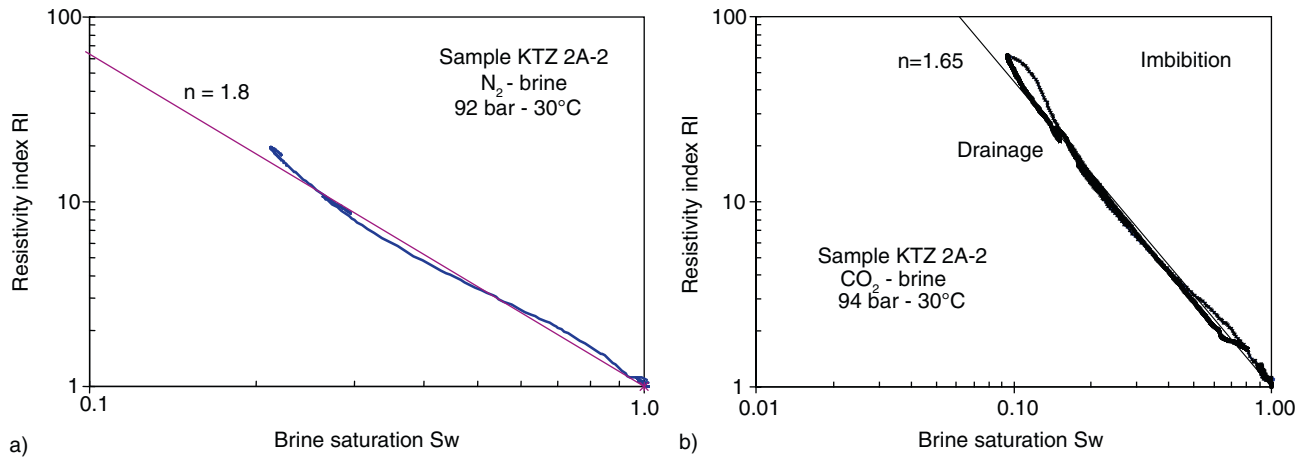


Figure 16

Resistivity index curve at storage conditions for a sample of the lower zone. a) N₂-brine system. b) CO₂ – brine system. The saturation exponent *n* is smaller (1.65) than in the N₂ – brine experiment.

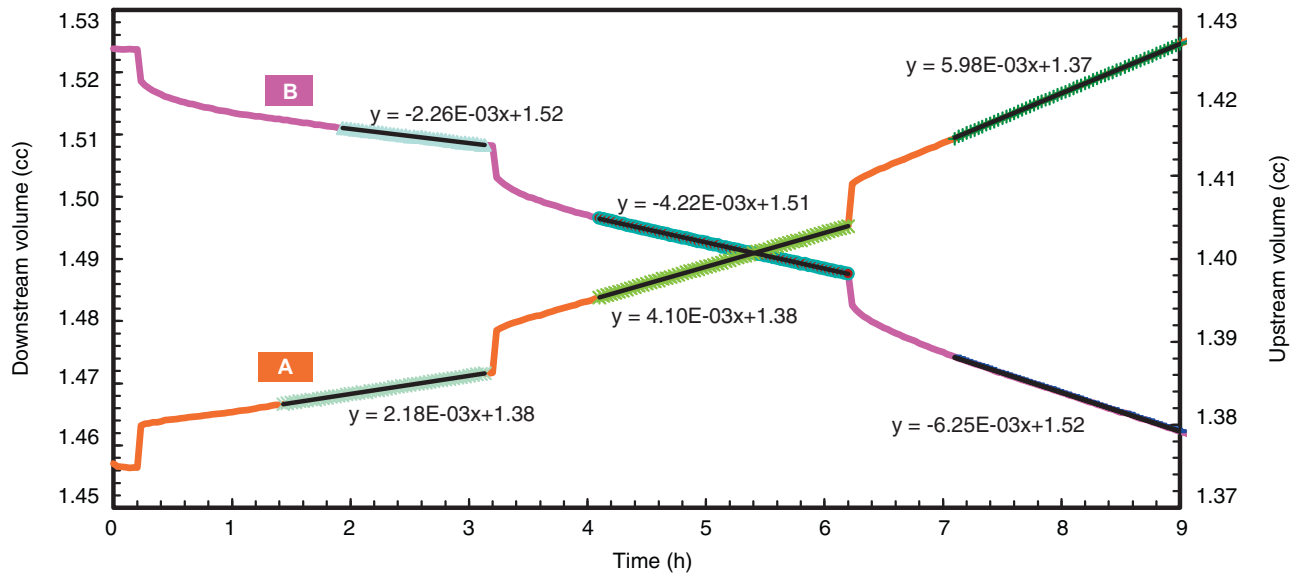


Figure 17

Measurement of the piston strokes during “push-pull” on the caprock sample CR-KTZ 1b.

pressure gradient ($P_u - P_d$) (Fig. 18), the three measured points align along a slope proportional to the permeability, according to Equation (6). It is also observed that the permeability obtained from upstream and downstream flow rates are identical (Tab. 3), confirming effectively that the flow reached a steady state. An average permeability of 27.4 nD was estimated. This value is much lower than previously published in the mD range. This strong disagreement may be due to the presence of micro-fractures induced frequently during the preparation and handling of argillaceous caprock samples. Indeed,

on one of the tested caprock samples, we found a permeability in the mD range due to the presence of visible fractures.

A pulse decay experiment (Fig. 19) was also performed with water, using an initial pore pressure of 7 MPa and a pulse pressure of 8.9 MPa. Upstream pressure decreases while downstream pressure increased until equilibrium at a pressure of 7.55 MPa. The experiment lasted ten hours. Numerical simulations of Equation (7) were performed using the permeability of 27.4 nD determined in the previous steady state experiment,

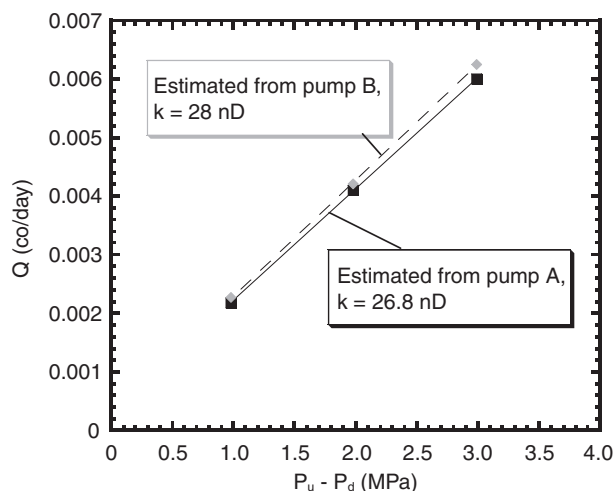


Figure 18

Evolution of the water fluxes with the pressure gradient on the caprock sample CR-KTZ 1b.

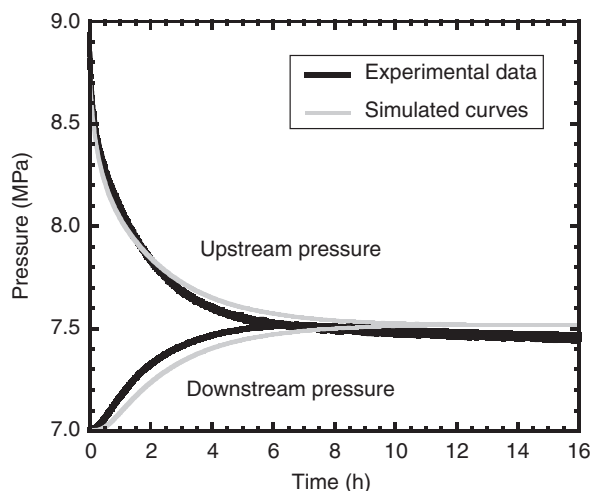


Figure 19

Results of the pulse decay experiment on the caprock sample CR-KTZ 1b (Experimental data and best fit simulations).

TABLE 3
Characteristics of the caprock sample CR-KTZ 1b

Sample CR-KTZ 1b		
Diameter		4.01 cm
Section		12.63 cm ²
Length		6.46 cm
Permeability and storage factor		
Permeability from upstream volume	From steady state	26.8 nD
Permeability from downstream volume		28 nD
Mean permeability		27.4 nD
Storage factor	From pulse test	1.1 × 10⁻⁶ m⁻¹

the fitting parameter being the specific storage S_s . The S_s value obtained by this procedure is $1.1 \times 10^{-6} \text{ m}^{-1}$ (Fig. 19). The simulated curve fairly described the experimental data. The difference can be explained by: anisotropy of the sample since the pulse decay within an Hassler cell is not entirely a 1D problem, possible leakage (upstream pressure after 10 h is slightly lower than downstream pressure), and an overestimation of the storage factor of the downstream reservoir at a mean pressure of 7.5 MPa. More details on how pulse decay can differ to steady state experiment are presented in Boulin *et al.* (2011).

Entry Pressure

Using the standard method (step by step), a first attempt was made to determine the nitrogen entry pressure. The sample was initially maintained at *in situ* conditions with a confining stress of 10 MPa and a pore pressure of 3 MPa. At the inlet, gas pressure was increased by 1 MPa each week up to 7 MPa but no production was observed at the outlet, even after a period of two weeks. The entry pressure is therefore higher than 7 MPa. However, higher pressure cannot be tested because microcracks may appear when upstream pressure is close to the confining stress (Skutveit *et al.*, 2009).

It was thus decided to increase the confining pressure to 30 MPa in order to be able to increase the inlet gas pressure. As a consequence, the permeability decreases from 28 nD down to 16.5 nD. Then, the experiment was repeated using an initial gas pressure of 10 MPa, with an increment of 1 MPa every three to five days. The experiment lasted 48 days and despite the long time steps, it was rather difficult to estimate when the production of water started (Fig. 20). A slight volume change suggest that water production is occurring in the middle of the 15.9 MPa step. A longer pressure step (at least 5 more days) would have been required to confirm that. At least, the gas penetrated undoubtedly the sample for a gas pressure higher than $15.4 \text{ MPa} \pm 10\%$. Subtracting the pore pressure, P_E was thus estimated at $10.4 \text{ MPa} \pm 15\%$. This value is further discussed below.

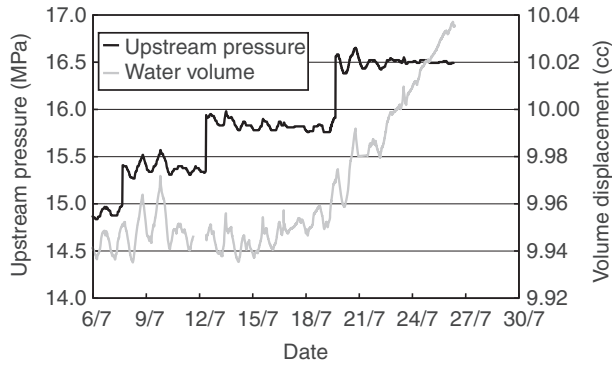


Figure 20

Water production during the step by step approach on the caprock sample CR-KTZ 1b.

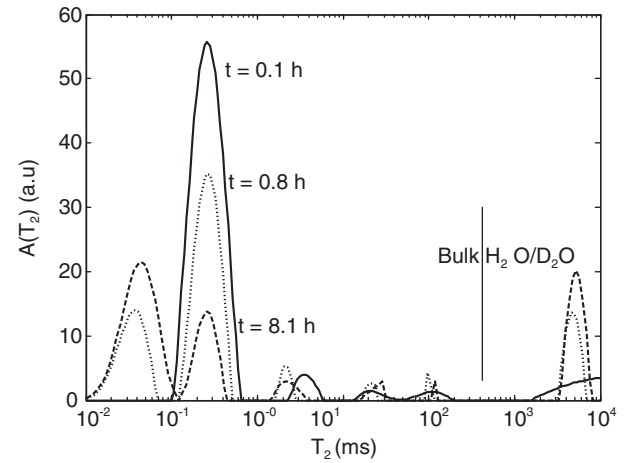


Figure 21

T_2 distribution at different times in the D₂O diffusion experiment. Caprock sample CR KTZ 2A, porosity 21%.

For comparison, the dynamic method was performed afterwards. The sample was resaturated with water. Gas pressure at the inlet was set at 18.6 MPa ($\Delta P = P_g - P_w = 16.0$ MPa). Two different flow rates were observed, before and after gas in contact with the sample, and were respectively 1 cc/day and 0.15 cc/day. The entry pressure value is therefore 13 MPa \pm 12%. More details on how the entry pressure were done on the sample CR-KTZ are available in Boulin *et al.* (2011). Here, the total duration is 3 days but this much more rapid measurement is only possible when the initial gas pressure is properly chosen.

The value obtained by the two techniques here is close to 12 MPa and is representative of a sample at an effective stress of 25 MPa which is higher than the *in situ* stress estimated at 10 MPa. To correct for the stress effect, a relationship between permeability and entry pressure can be used:

$$P_e \sim k^{-0.5} \quad (15)$$

In the above relationship, as in a capillary tube, the entry pressure P_e is assumed to be related to a mean pore diameter d , and the permeability k is assumed to be proportional to d^2 . This is similar to the empirical relationship proposed by Thomas *et al.* (1968). If the confinement reduces the pore mean diameter d and does not affect the internal structure or connectivity of the porous structure, relation (15) is valid. Since permeability is reduced from 28 nD (at *in situ* stress) to 16.5 nD, the entry pressure should have been increased likewise. The entry pressure measured at an effective pressure of 25 MPa ($P_e = 12$ MPa) is indeed higher than the *in situ* P_e value. Using relation (15), the *in situ* P_e is 9 MPa.

Finally, a conversion to the CO₂/brine system must be performed. For CO₂, the P_e value will be lower due to a lower interfacial tension compared to the nitrogen/brine one. The *in situ* pore pressure is higher than 5 MPa and therefore CO₂ pressure will be higher than 5 MPa. In this range of pressure, interfacial tension for CO₂/brine can be assumed constant (close to 28 mN/m, Chalbaud *et al.*, 2010). Assuming an interfacial tension of 73 mN/m for the nitrogen/brine system, the estimated P_e value for CO₂ is thus 3.5 MPa.

Diffusion

The relaxation data plotted for three different time (Fig. 21) shows the decrease of the main peak ($T_2 = 0.25$ ms) containing most of the porous volume. Some minor peaks below 1 000 ms representing larger pores in small quantities are also present. Water diffusing outside the sample is characterized by longer relaxation times (above 1 000 ms) and its contribution is not taken into account in the magnetization decay curve.

From the magnetization decay curve, the fitted pore diffusivity D_p is 0.8×10^{-9} m²/s at 30°C (Fig. 22, the porosity of the sample is 21%). The bulk water diffusivity D_0 at the same temperature is 2.6×10^{-9} m²/s. This result is coherent with an Archie relation of the form:

$$\frac{D_p}{D_0} = \phi^{m-1} \quad (15)$$

where $m = 1.77$ is the cementation exponent usually derived from electrical measurements. Such coherence

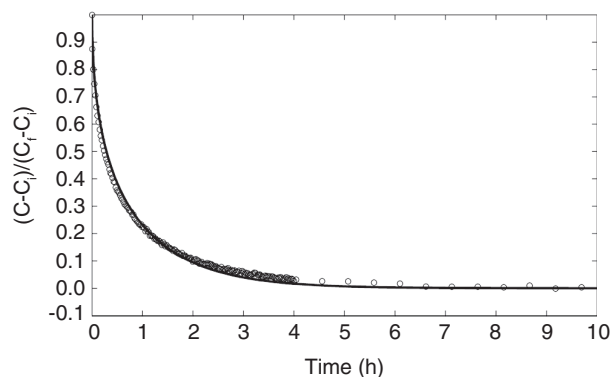


Figure 22

Analysis of D₂O NMR diffusion experiments on sample CR KTZ 2A. The line is the best using Equation (9), yielding a diffusion coefficient of $8.1 \times 10^{-6} \text{ cm}^2/\text{s}$ at 30°C.

was also found in other situations (Berne *et al.*, 2010), confirming that formation factor measurements are also good estimators of effective diffusivities.

CONCLUSION

The series of experiments shown in this work are examples of how a storage site can be characterized from a petrophysical point of view without excessive experimental complexity, to provide data beyond porosity and permeability. First, log data should be examined not only qualitatively for lithological description but also quantitatively. Beside porosity, we suggest here that NMR logs, preferably measured with a water based mud, should be performed systematically because they provide a unique information about pore size distribution that can be compared directly to laboratory experiments. In an aquifer, NMR can provide after laboratory calibration a continuous irreducible water saturation information in the storage zone that can be used later to build flow units in conjunction with lithology. In the present case, we did not use NMR logs to estimate fluctuations of permeability but this is also a possible use. For the formation studied, irreducible saturation is determined by the clay content and the measured NMR cut-off of 8 ms is a clear indication of this observation. Resistivity properties are also affected by the presence of clays, with m and n exponents close to 1.7.

For the determination of transport properties, we suggest to use the centrifuge technique to measure at the same time air-brine first drainage capillary pressure and water

relative permeability curves in the largest saturation range possible (from 1 down to *Swirr*). This is a simple first approach giving without ambiguity water relative permeability curves on several samples, a key parameter for numerical simulation. After that, other experiments such as steady state or unsteady state flooding can be performed to provide data at storage conditions to complete the information. For the formation considered, capillary pressure measurements indicate that the smallest *in situ* water saturation that can be reached is about 20% for the lower zone and 28% for the upper reservoir zone. For the upper zone, both relative permeability and resistivity curves present a peculiar behavior in the saturation range above 0.8, *i.e.* a sharp increase of resistivity and a sharp decrease of relative water permeability compared to usual behavior. This is not observed on the lower zone in which a smoother curve is observed. The two different behaviors are most likely linked to the different clay amount and distribution as observed on CT scans. A recent and very versatile *Kr* model (LET functions) had to be used to describe the relative permeability curves in the full saturation range.

The measured resistivity properties are useful for the interpretation of resistivity monitoring and the prediction of CO₂ invasion and saturation during injection. The presented results establish a relationship to convert resistivity distributions into saturation profiles in the reservoir target zone as well as in the caprock region. At storage conditions with CO₂, the saturation exponent n decreases slightly from 1.8 down to 1.65 when replacing N₂ by CO₂. This effect has been observed in another experimental program with clayey sandstones and need further work to be fully understood.

For the caprock zone, we evaluated water permeability using a steady state technique that required typically an experimental time of 1 day. Water diffusivity was estimated using a simple NMR tracer technique requiring typically less than 1 day. Entry pressure, useful for the prediction of CO₂ migration into the caprock is a more difficult experiment and can require weeks to months, depending on the requested accuracy. For the mudstone studied, we found a water permeability of 27 nD ($27 \times 10^{-21} \text{ m}^2$) instead of much larger values previously published in the mD range. The water diffusivity measured by NMR techniques on one sample is $0.8 \times 10^{-9} \text{ m}^2/\text{s}$, 3.2 times less than free water, in agreement with a simple Archie model using $m = 1.8$. It can be used as an upper limit for the diffusivity of dissolved CO₂ in water. The CO₂ entry pressure at representative confining stress is about 3.5 MPa.

Finally, we can establish that the deployed integrated petrophysical characterization has been successfully demonstrated for Ketzin site samples from the cored

reservoir and caprock section. The suggested best-practice workflow presents an instrument to improve the coherency of the experimental data and it contributes to the necessary conversion of measured resistivity field data into CO₂ saturation distribution as well.

In general, the integrated petrophysical characterization supports the link between geophysical monitoring and fluid-flow modeling, and represents itself as indispensable tool in the phase of data integration of a CO₂ storage site.

ACKNOWLEDGMENTS

The authors thank the French National Research Agency (ANR) for supporting this research in the framework of the COSMOS-2 project, which was connected with the German COSMOS project (CO₂ Storage, Monitoring and Safety Technologies) via the Eurogia programme. P. Poulain, F. Norrant and Y. Larabi from IFPEN contributed also to the data acquisition in the experimental program. E. Brosse from IFPEN contributed also to the improvement of the final manuscript.

REFERENCES

- Bauget F., Gautier S., Lenormand R., Samouillet A. (2012) Gas-liquid relative permeability from one-step and multi-step centrifuge experiments, *International Symposium of the Society of Core Analysts*, 27-30 Aug., Aberdeen, United Kingdom, available at <http://www.scaweb.org/>.
- Bennion B., Bachu S. (2008) Drainage and imbibition relative permeability relationships for supercritical CO₂/brine and H₂S/brine systems in intergranular sandstone, carbonate, shale, and anhydrite rocks, *SPE Reserv. Eval. Eng.* **11**, 3, 487-496.
- Bergmann P., Lengler U., Schmidt-Hattenberger C., Giese R., Norden B. (2010) Modelling the geoelectric and seismic reservoir response caused by carbon dioxide injection based on multiphase flow simulation: Results from the CO₂SINK project, *Chem. Erde* **70**, 3, 173-183.
- Berne Ph, Bachaud P., Fleury M. (2010) Diffusion properties of carbonated caprocks from the Paris Basin, *Oil Gas Sci. Technol.* **65**, 3, 473-484.
- Beutler G., Nitsch E. (2005) Paläographischer Überblick, in *Stratigraphie von Deutschland IV, Keuper*, Beutler G. et al. (eds) **253**, 15-30, Courier Forschungsinstitut Senckenberg, Stuttgart.
- Boulin P.F., Bretonnier P., Gland N., Lombard J.M. (2012) Contribution of steady state methods to water permeability measurement in very low permeability porous media, *Oil Gas Sci. Technol.* **67**, 3, 387-401.
- Boulin P.F., Bretonnier P., Vassil V., Samouillet A., Fleury M., Lombard J.M. (2011) Entry pressure measurements using three unconventional experimental methods, *International Symposium of the Society of Core Analysts*, 18-21 Sept., Austin, USA, SCA2011-02.
- Brace W.F., Walsh J.B., Frangos W.T. (1968) Permeability of Granite under High Pressure, *J. Geophys. Res.* **73**, 6, 2225-2236.
- Chalbaud C., Robin M., Lombard J.M., Bertin H., Egermann P. (2010) Brine/CO₂ Interfacial Properties and Effects on CO₂ Storage in Deep Saline Aquifers, *Oil Gas Sci. Technol.* **65**, 4, 541-555.
- Christensen N.B., Sherlock D., Dodds K. (2006) Monitoring CO₂ injection with cross-hole electrical resistivity tomography, *Explor. Geophys.* **37**, 44-49.
- Dullien F.A.L. (1992) *Porous Media Fluid Transport and Pore Structure*, 2nd ed., Academic Press, San Diego, pp. 333-486.
- Egermann P., Lombard J.-M., Bretonnier P. (2006) A fast and accurate method to measure threshold capillary pressure of caprocks under representative conditions, *International Symposium of the Society of Core Analysts*, 12-16 Sept., Trondheim, Norway, available at <http://www.scaweb.org/>, SCA2006-07.
- Fleury M. (1998) FRIM: a Fast Resistivity Index Measurement Method, *International Symposium of the Society of Core Analysts*, 14-16 Sept., The Hague, The Netherlands, available at <http://www.scaweb.org/>.
- Fleury M., Poulain P., Ringot G. (1998) A capacitance technique for measuring production while centrifuging, *International Symposium of the Society of Core Analysts*, 14-16 Sept., The Hague, The Netherlands, available at <http://www.scaweb.org/>, SCA-9833.
- Fleury M., Liu F. (2000) Frequency effect on resistivity index curves using a new method, *41st Annual SPWLA Symposium*, 4-7 June, Dallas, USA.
- Fleury M. (2003) Advances in Resistivity Measurements using the FRIM Method at Reservoir Conditions. Applications to Carbonates, *International Symposium of the Society of Core Analysts*, 21-24 Sept., Pau, France, available at <http://www.scaweb.org/>, SCA2003-31.
- Fleury M. (2007) NMR surface relaxivity determination using NMR apparent diffusion curves and BET measurements, *International Symposium of the Society of Core Analysts*, 10-12 Sept., Calgary, Canada, available at <http://www.scaweb.org/>, SCA2007-35.
- Fleury M., Berne P., Bachaud P. (2009) Diffusion of dissolved CO₂ in caprock, *Energy Procedia* **1**, 3461-3468.
- Forbes P.L (1991) Simple and Accurate Methods for Converting Centrifuge Data into Drainage and Imbibition Capillary Pressure Curves, *International Symposium of the Society of Core Analysts*, London, England, available at <http://www.scaweb.org/>, SCA Conference Paper Number 9107.
- Förster A., Norden B., Zinck-Jørgensen K., Frykman P., Kulenkampff J., Spangenberg E., Erzinger J., Zimmer M., Kopp J., Borm G., Juhlin C., Cosma C., Hurter S. (2006) Baseline characterization of the CO₂SINK geological storage site at Ketzin, Germany, *Environ. Geosci.* **133**, 145-161.
- Förster A., Schöner R., Förster H.-J., Norden B., Blaschke A.-W., Luckert J., Beutler G., Gaupp R., Rhede D. (2010) Reservoir characterization of a CO₂ storage aquifer: The Upper Triassic Stuttgart Formation in the Northeast German Basin, *Mar. Petrol. Geol.* **27**, 2156-2172.
- Giese R., Henniges J., Lüth S., Morozova D., Schmidt-Hattenberger C., Würdemann H., Zimmer M., Cosma C., Juhlin C., CO₂SINK Group (2009) Monitoring at the CO₂SINK Site: A Concept Integrating Geophysics Geochemistry and Microbiology, *Energy Procedia* **1**, 1, 2251-2259.

- Girard J.-F., Coppo N., Rohmer J., Bourgeois B., Naudet V., Schmidt-Hattenberger C. (2011) Time-lapse CSEM monitoring of the Ketzin (Germany) CO₂ injection using 2×MAM configuration, *Energy Procedia* **4**, 3322-3329.
- Han M., Fleury M., Levitz P. (2007) Effect of the pore structure on resistivity index curves, *International Symposium of the Society of Core Analysts*, 10-13 Sept., Calgary, Canada, available at <http://www.scaweb.org/>, SCA2007-34.
- Honarpour M., Koederitz L., Harvey A.H. (1986) *Relative permeability of Petroleum Reservoir*, CRC Press, Boca Raton, Florida.
- Kummerow J., Spangenberg E. (2011) Experimental evaluation of the impact of the interactions of CO₂-SO₂, brine, and reservoir rock on petrophysical properties: A case study from the Ketzin test site, Germany, *Geochem. Geophys. Geosyst.* **12**, Q05010.
- Kiessling D., Schmidt-Hattenberger C., Schuett H., Schilling F., Krueger K., Schoebel B., Danckwardt E., Kummerow J., CO₂SINK Group (2010) Geoelectrical methods for monitoring geological CO₂ storage: First results from cross-hole and surface-downhole measurements from the CO₂SINK test site at Ketzin (Germany), *Int. J. Greenhouse Gas Control* **4**, 5, 816-826.
- Lenormand R. (2003) Interpretation of mercury injection curves to derive pore size distribution, *International Symposium of the Society of Core Analysts*, 21-24 Sept., Pau, France, available at <http://www.scaweb.org/>, SCA2003-52.
- Li S., Dong M., Li Z., Huang S., Qing H., Nickel E. (2005) Gas breakthrough pressure for hydrocarbon reservoir seal rocks: implications for the security of a long-term CO₂ storage in the Weyburn field, *Geofluids* **5**, 326-334.
- Lomeland F., Ebeltoft E., Hammervold Thomas W. (2005) A New Versatile Relative Permeability Correlation, *International Symposium of the Society of Core Analysts*, 21-25 August, Toronto, Canada, available at <http://www.scaweb.org/>, SCA2005-32.
- Martens S., Liebscher A., Möller F., Würdemann H., Schilling F., Kühn M., Ketzin Group (2011) Progress report on the first European on-shore CO₂ storage site at Ketzin (Germany) – Second year of injection, *Energy Procedia* **4**, 3246-3253.
- Nakatsuka Y., Xue Z., Garcia H., Matsuoka T. (2010) Experimental study on CO₂ monitoring and quantification of stored CO₂ in saline formations using resistivity measurements, *Int. J. Greenhouse Gas Control* **4**, 209-216.
- Norden B., Förster A., Vu-Hoang D., Marcellis F., Springer N., Le Nir I. (2010) Lithological and petrophysical core-log interpretation in the CO₂SINK, the European CO₂ onshore research storage and verification project, *SPE J.* **13**, 2, 179-192.
- Prevedel B., Wohlgenuth L., Henniges J., Krüger K., Norden B., Förster A., CO₂SINK Drilling Group (2008) The CO₂SINK boreholes for geological storage testing, *Scientific Drilling* **6**, 32-37.
- Prevedel B., Wohlgenuth L., Legarth B., Henniges J., Schütt H., Schmidt-Hattenberger C., Norden B., Förster A., Hurter S. (2009) The CO₂SINK boreholes for geological CO₂-storage testing, *Energy Procedia* **1**, 1, 2087-2094.
- Ramirez A.L., Newmark R.L., Daily W.D. (2003) Monitoring Carbon Dioxide Floods Using Electrical Resistance Tomography (ERT): Sensitivity Studies, *J. Environ. Eng. Geophys.* **8**, 3, 187-208.
- Schilling F., Borm G., Würdemann H., Möller F., Kühn M., CO₂SINK Group (2009) Status Report on the First European on-shore CO₂ Storage Site at Ketzin (Germany), *Energy Procedia* **1**, 1, 2029-2035.
- Schmidt-Hattenberger C., Bergmann P., Kießling D., Krüger K., Rücker C., Schütt H., Ketzin Group (2011a) Application of a Vertical Electrical Resistivity Array (VERA) for monitoring CO₂ migration at the Ketzin site: First performance evaluation, *Energy Procedia* **4**, 3363-3370.
- Schmidt-Hattenberger C., Bergmann P., Labitzke T., Schröder S., Krüger K., Rücker C., Schütt H. (2011b) A modular geoelectrical monitoring system as part of the surveillance concept in CO₂ storage projects, *Energy Procedia* **23**, 400-407.
- Skurtveit E., Aker E., Angeli N., Soldal M. (2009) Coupled flow geomechanical testing of low permeable material – Application for CO₂ storage, *2nd International Conference on Fault and Top Seals*, 21-24, Sept., Montpellier, France.
- Streich R., Becken M., Matzander U., Ritter O. (2011) Strategies for land-based controlled-source electromagnetic surveying in high-noise regions, *Leading Edge* **30**, 1174-1181.
- Thomas L.K., Katz D.L., Tek M.R. (1968) Threshold pressure phenomena in porous media, *SPE J.* **243**, 174-184.
- Zemke K., Liebscher A., Wandrey M., CO₂SINK Group (2010) Petrophysical analysis to investigate the effects of carbon dioxide storage in a subsurface saline aquifer at Ketzin, Germany (CO₂SINK), *Int. J. Greenhouse Gas Control* **4**, 6, 990-999.
- Würdemann H., Moeller F., Kuehn M., Heidug W., Christensen N.P., Borm G., Schilling F.R., CO₂SINK Group (2010) CO₂SINK-From site characterisation and risk assessment to monitoring and verification: One year of operational experience with the field laboratory for CO₂ storage at Ketzin, Germany, *Int. J. Greenhouse Gas Control* **4**, 6, 938-951.

Final manuscript received in November 2012

Published online in June 2013

Copyright © 2013 IFP Energies nouvelles

Permission to make digital or hard copies of part or all of this work for personal or classroom use is granted without fee provided that copies are not made or distributed for profit or commercial advantage and that copies bear this notice and the full citation on the first page. Copyrights for components of this work owned by others than IFP Energies nouvelles must be honored. Abstracting with credit is permitted. To copy otherwise, to republish, to post on servers, or to redistribute to lists, requires prior specific permission and/or a fee: Request permission from Information Mission, IFP Energies nouvelles, fax. +33 1 47 52 70 96, or revueogst@ifpen.fr.